Research Square

Preprints are preliminary reports that have not undergone peer review.
They should not be considered conclusive, used to inform clinical practice,
or referenced by the media as validated information.

Distinct phenotypic and transcriptomic profiles of myeloid-derived suppressor cells induced by 4T1 tumor growth and cyclophosphamide treatment

Maysa M. Abosenna
Egypt-Japan University of Science and Technology
Asmaa M. Youssef
Nagoya City University Graduate School of Medical Sciences
Ahmed M. Moustafa
Nagoya City University Graduate School of Medical Sciences
Motoharu Hamada
Nagoya City University Graduate School of Medical Sciences
Ahmed Osman
Egypt-Japan University of Science and Technology
Ahmed M.R. Fath El-Bab
Egypt-Japan University of Science and Technology
Essam Elshikh
Tanta Cancer Center
Mona Sheta
Cairo University
Yousef Mysara
Ain Shams University
Somaia M. Zakzok
Nagoya City University Graduate School of Medical Sciences
Kazi Mahnaz Mehrin
Nagoya City University Graduate School of Medical Sciences
Mei Suzuki
Nagoya City University Graduate School of Medical Sciences
Mohamed L. Salem
Tanta University
Hisashi Oishi
hoishi@med.nagoya-cu.ac.jp

Nagoya City University Graduate School of Medical Sciences

Research Article

Keywords: myeloid-derived suppressor cells, 4T1, cyclophosphamide, RNA sequencing, reactive oxygen species, nitric oxide

Posted Date: September 13th, 2026

DOI: https://doi.org/10.21203/rs.3.rs-10764275/v1

License: This work is licensed under a Creative Commons Attribution 4.0 International License. Read Full License

Additional Declarations: No competing interests reported.

Abstract

Myeloid-derived suppressor cells (MDSCs) are a heterogeneous population of immature myeloid cells that expand under pathological conditions. They mediate immunosuppression through multiple mechanisms, including arginase activity, nitric oxide (NO) production, reactive oxygen species (ROS) generation, and immunoregulatory cytokine secretion. Although tumor-bearing models are widely used to induce MDSC accumulation *in vivo*, cyclophosphamide (CTX) administration can also promote MDSC expansion under specific dosing conditions. However, whether tumor growth and CTX treatment generate phenotypically and molecularly distinct MDSC populations remains unclear. To address this question, we compared bone marrow CD11b^{+}Gr-1^{+} MDSCs induced by 4T1 tumor growth, CTX treatment, or their combination. We assessed their subset composition, expression of MDSC-associated genes, immunosuppressive mediator profiles, and transcriptomic characteristics. 4T1 tumor growth preferentially expanded polymorphonuclear MDSCs, whereas CTX treatment preferentially expanded monocytic MDSCs. qRT-PCR analysis showed increased *Cybb* and *Nos2* expression in cells from 4T1 tumor-bearing mice, whereas cells from CTX-treated mice exhibited relatively limited changes in the selected MDSC-associated genes. Notably, the combination group was characterized by selective upregulation of *Cd84* and *Tgfb1*. Relative ROS fluorescence was numerically increased in all induction groups compared with the Control group, with the highest values observed in the tumor-containing groups. Flow cytometric analysis suggested increased NO-associated fluorescence in the CTX-containing groups. RNA sequencing clearly distinguished all induction groups and revealed condition-specific transcriptional programs. Together, these findings indicate that tumor growth, CTX treatment, and their combination generate MDSC populations with distinct subset compositions, mediator-associated profiles, and transcriptional programs, underscoring the importance of the induction method when interpreting MDSC phenotypes.

Introduction

Myeloid-derived suppressor cells (MDSCs) are a heterogeneous population of myeloid cells that play critical roles in immune regulation (1). They arise through dysregulated myelopoiesis that impairs the maturation of myeloid progenitors and, in some contexts, through the reprogramming of mature myeloid cells. Their expansion and suppressive activity are further shaped by inflammatory and tumor-derived signals, including GM-CSF, G-CSF, and IL-6 (2). MDSCs exert potent immunosuppressive activity and are known to promote tumor immune evasion and resistance to immunotherapy by suppressing T-cell responses. In mice, MDSCs are commonly identified as CD11b^{+}Gr-1^{+} myeloid cells and are further classified into two major subsets: monocytic MDSCs (M-MDSCs), characterized as CD11b^{+}Ly6G^{-}Ly6C^{hi}, and polymorphonuclear MDSCs (PMN-MDSCs), characterized as CD11b^{+}Ly6G^{+}Ly6C^{low} (3). These subsets exhibit considerable phenotypic and functional plasticity (4). Importantly, MDSCs are characterized by both their phenotypic features and immunosuppressive activity (3, 5).

MDSCs expand under diverse pathological conditions, including cancer, chronic inflammation, and autoimmune diseases, and may also be induced pharmacologically by cyclophosphamide (2, 6).

Although these MDSCs share fundamental immunosuppressive properties, the signals present in each environment may confer distinct molecular and functional characteristics. These context-dependent differences may reflect distinct suppressive mechanisms, including reactive oxygen species (ROS) generation, nitric oxide (NO) production, arginase-1 activity, and transforming growth factor-β (TGF-β) secretion. Accordingly, MDSC phenotype and function may vary across different induction environments. MDSCs identified by similar surface markers may therefore differ substantially in their suppressive mediators, lineage composition, and transcriptional state depending on the induction method.

A variety of murine tumor models, including EL-4 thymoma, Lewis lung carcinoma (3LL), B16-F10 melanoma, and 4T1 mammary carcinoma, have been reported to promote MDSC accumulation *in vivo* (7–9). Tumor-derived inflammatory and myelopoietic factors can promote MDSC expansion and frequently favor the accumulation of PMN-MDSCs, which often exhibit ROS-dependent suppressive activity (10, 11). In contrast, the chemotherapeutic agent CTX can induce transient bone marrow injury and lymphopenia, followed by compensatory hematopoietic recovery, during which M-MDSCs with NO-dependent immunosuppressive activity may expand (6, 12, 13). However, differences between tumor-induced and CTX-induced MDSCs in subset composition, suppressive properties, and gene expression profiles remain poorly understood. Clarifying these differences is important for understanding the biological diversity of MDSCs generated under different induction conditions.

In this study, we compared bone marrow MDSCs from 4T1 tumor-bearing mice, CTX-treated mice, and mice receiving both interventions, focusing on their subset composition and suppressive mediator profiles. We further performed RNA sequencing to characterize induction-specific gene expression profiles and examine how these profiles corresponded to the observed differences in MDSC subsets and suppressive mediators.

Materials and Methods

4T1 cell culture. The mouse mammary tumor cell line 4T1-Luc was obtained from the JCRB Cell Bank and maintained as a monolayer in RPMI-1640 (Thermo Fisher Scientific, Waltham, MA, USA) supplemented with 10% heat-inactivated fetal bovine serum (Thermo Fisher Scientific) and 1% penicillin-streptomycin (FUJIFILM Wako Pure Chemical, Osaka, Japan). Cells were grown at 37 °C in a humidified incubator with 5% CO_2 and harvested at 50 − 70% confluence.

Animals. All animal experiments were approved by the Institutional Animal Care and Use Committee (IACUC) of Nagoya City University, Japan (Approval No. 25–041), and were conducted in accordance with institutional guidelines for animal care and use. Female BALB/c mice (6 − 8 weeks of age) were purchased from Japan SLC (Shizuoka, Japan), and maintained under specific pathogen-free conditions. Mice were housed in a 12-h light/12-h dark cycle at a standard temperature of 22 ± 2°C and were provided standard chow and water *ad libitum*.

MDSC induction. Mice were randomly assigned to four groups: control, tumor-bearing (Tumor), cyclophosphamide-treated (CTX), and tumor-bearing plus cyclophosphamide-treated (Tumor + CTX)

(Fig. 1A). For tumor inoculation, 4T1-Luc cells were bilaterally injected into the mammary fat pads adjacent to the third nipples at 1×10^5 cells in 50 µL PBS per site. In the CTX group, cyclophosphamide (Merck, Darmstadt, Germany) was administered intraperitoneally at 150 mg/kg 7 days before MDSC isolation (12, 14). In the Tumor + CTX group, 4T1-Luc cells were inoculated on day 0, and CTX was administered 8, 12, and 16 days after tumor inoculation. Control mice received bilateral mammary fat pad injections of 50 µL PBS per site. Mice were euthanized and bone marrow cells were collected according to the schedule shown in Fig. 1A.

Euthanasia, bone marrow harvesting and isolation of MDSCs. At the designated experimental endpoint, mice were euthanized by CO_2 inhalation. CO_2 exposure was continued until the animals became unconscious and respiration had ceased, after which cervical dislocation was performed as a secondary method to ensure death. No separate anaesthetic agent was administered before euthanasia. Bone marrow cells were collected by flushing each femur and tibia with 500 µL of cold PBS using a 23-gauge needle. After red blood cell lysis with ACK buffer for 3 min at room temperature, the remaining cells were washed twice with PBS. MDSCs were then isolated using the EasySep Mouse MDSC (CD11b+Gr1+) Isolation Kit according to the manufacturer's instructions (ST-19867; STEMCELL Technologies, Vancouver, BC, Canada). The isolated cell fractions were used for subsequent analyses.

Flow cytometry. Isolated cells were incubated with Mouse BD Fc Block (BD Biosciences, San Jose, CA, USA) for 15 min at 4°C and then stained for 30 min at 4°C in the dark with FITC-conjugated anti-mouse CD11b (M1/70), BV421-conjugated anti-mouse Ly-6C (HK1.4), and PE-conjugated anti-mouse Ly-6G (1A8) antibodies (all from BioLegend, San Diego, CA, USA). After washing twice with PBS containing 1% FBS, cells were resuspended and stained with 7-AAD (BD Biosciences) to assess viability. Viable $CD11b^+$ cells were classified as $Ly6G^+Ly6C^{low}$ PMN-MDSCs or $Ly6G^-Ly6C^{high}$ M-MDSCs. Data were acquired using a BD FACSCanto II flow cytometer (BD Biosciences) and analyzed with FlowJo software (BD Biosciences).

RNA extraction and quality control. Total RNA was extracted using the FastGene RNA Premium Kit (Nippon Gene, Tokyo, Japan) according to the manufacturer's instructions. RNA concentration was measured using a NanoDrop One spectrophotometer (Thermo Fisher Scientific). Only samples meeting the following criteria were used for subsequent experiments: an $A_{260}/A_{280} > 1.8$ and, for RNA-seq, an RNA Integrity Number (RIN) > 7.0 as determined by an Agilent 2100 Bioanalyzer (Agilent Technologies, Santa Clara, CA, USA).

Quantitative RT-PCR. Total RNA (1 µg) was reverse-transcribed into cDNA using the QuantiTect Reverse Transcription Kit (Qiagen, Hilden, Germany). Quantitative real-time PCR was performed using PowerUp SYBR Green Master Mix (Thermo Fisher Scientific) on a QuantStudio 12K Flex Real-Time PCR System (Thermo Fisher Scientific). Gene expression levels were normalized to *Hprt* and calculated using the $2^{-\Delta\Delta Ct}$ method. Primer sequences are listed in Supplementary Table 1.

Measurement of intracellular oxidative activity. Intracellular oxidative activity was assessed using an Intracellular Reactive Oxygen Species Detection Assay Kit (Tokyo Kasei Kogyo, Tokyo, Japan) according to the manufacturer's instructions. Briefly, cells were incubated with the oxidation-sensitive dye DCFH-DA, and signal intensity was measured using a microplate reader at excitation and emission wavelengths of 485 nm and 520 nm, respectively (SpectraMax Gemini EM, Molecular Devices, San Jose, CA, USA).

Measurement of nitric oxide. Nitric oxide (NO) production was assessed using Diaminofluorescein-FM diacetate (DAF-FM DA; Goryo Chemical, Sapporo, Japan). Cells were incubated with 10 μmol/L DAF-FM DA in PBS (pH 7.2) for 60 min at 37°C, washed, and then incubated for an additional 15 min to allow complete de-esterification of the intracellular diacetates. DAF-FM fluorescence was analyzed using a BD FACSCanto II flow cytometer (BD Biosciences) and FlowJo software (BD Biosciences).

Arginase activity. Arginase activity was determined using an Arginase Activity Assay Kit (AK89N, Cosmo Bio, Tokyo, Japan) according to the manufacturer's instructions. Briefly, 2×10^5 MDSCs were lysed and incubated with the reaction mixture supplied with the kit. Absorbance was measured at 540 nm with a microplate reader (SpectraMax L, Molecular Devices). A standard curve was generated from the mean absorbance values of urea standards at each concentration using a linear regression, and arginase activity (U/mL) was calculated from the urea concentration of each sample according to the manufacturer's instructions. The activity was expressed per 2×10^5 cells.

RNA-seq analysis. Strand-specific RNA-seq libraries were prepared from total RNA using poly(A) mRNA enrichment, random hexamer priming, and dUTP-based second-strand synthesis, followed by adapter ligation and PCR amplification. The libraries were sequenced on the Illumina NovaSeq X Plus platform (150-bp paired-end; Novogene Co., Ltd., Beijing, China). All 16 libraries yielded a Q30 score ≥ 95%, with an average error rate of 0.01%. Raw reads were assessed using FastQC (v0.12.0; Andrews, 2010) and MultiQC (v1.32; Ewels et al., 2016). Low-quality reads and adapter sequences were trimmed using fastp (v1.0) to generate clean reads. Clean reads were then aligned to the mouse reference genome (GRCm39) using STAR (v2.7; Dobin et al., 2013) with GENCODE M38 annotation. The resulting BAM files were sorted, indexed, and evaluated with SAMtools (v1.23.1; Li et al., 2009) to assess mapping quality. Gene-level read counts were subsequently quantified using featureCounts (v1.6.4; Liao et al., 2014) in stranded paired-end mode (-s 2 -p), yielding the count matrix used for all downstream analyses.

Bioinformatics data analysis. Differential expression analysis was performed in R using the DESeq2 package. Genes that did not reach 10 counts in at least four samples were excluded from downstream analysis. Differentially expressed genes (DEGs) were identified based on an adjusted *P* value (padj) < 0.05 and absolute $\log_2$ fold change ($|\log_2 FC|$) > 1. Genes with padj < 0.05 and $\log_2 FC > 1$ were considered upregulated, whereas those with padj < 0.05 and $\log_2 FC < -1$ were considered downregulated. Exploratory analyses were conducted using variance-stabilizing transformation (VST)-normalized counts, including principal component analysis (PCA), sample-to-sample Euclidean distance heatmaps, and heatmaps of the top 1,000 most variable genes with per-gene z-score scaling. Data visualization was performed using the dplyr, ggplot2, ggrepel, EnhancedVolcano, pheatmap, and ggVennDiagram

packages. Volcano plots were generated to visualize differential gene expression patterns, and Venn diagrams were used to examine overlaps among differentially expressed gene sets. Functional enrichment analysis was conducted using the ShinyGO web-based platform with mouse gene identifiers. Upregulated and downregulated genes were analyzed separately, and significantly enriched KEGG pathways and Gene Ontology terms were identified using a false discovery rate (FDR) threshold of < 0.05.

Statistical analysis. Data are expressed as mean ± SEM. Statistical differences among multiple groups were evaluated using one-way ANOVA followed by Tukey's post hoc test. Differences were considered statistically significant at $P < 0.05$. Statistical analyses were carried out using GraphPad Prism 8.0.1 (GraphPad Software, San Diego, CA, USA).

Results

Expansion and subset composition of bone marrow MDSCs. All three induction conditions significantly increased both the absolute number and frequency of bone marrow MDSCs (Fig. 1B, C). Total leukocyte numbers were increased in the Tumor and Tumor + CTX groups, but not in the CTX group, suggesting that MDSC expansion may occur through different mechanisms in tumor-bearing and CTX-treated mice (Fig. 1D). Subset analysis revealed that 4T1 tumor inoculation preferentially increased PMN-MDSCs ($CD11b^{+}Ly6G^{+}Ly6C^{low}$), whereas CTX treatment and Tumor + CTX preferentially increased M-MDSCs ($CD11b^{+}Ly6G^{-}Ly6C^{hi}$) (Fig. 1E–G).

MDSC-associated and immunoregulatory gene expression. To further characterize the molecular features of MDSCs induced under different conditions, we examined the mRNA expression of MDSC-associated and immunoregulatory genes by quantitative RT-PCR (Fig. 2). Tumor-induced MDSCs exhibited significantly increased expression of *Cybb* and *Nos2* compared with the other groups, suggesting an increased potential for ROS- and NO production (Fig. 2A–B). In contrast, *Arg1* expression was significantly reduced in the Tumor and CTX groups compared with the Control group (Fig. 2C). Expression of *Cxcr2*, a chemokine receptor commonly associated with PMN-MDSCs, was significantly reduced in the CTX group (Fig. 2D). Overall, none of the examined genes showed significant upregulation in the CTX group relative to the Control group. Notably, the expression levels of *Tgfb1* and *Cd84* were significantly increased in the Tumor + CTX group, suggesting that the combined condition was associated with a distinct immunoregulatory gene expression profile (Fig. 2E–F). The expression levels of other MDSC-associated genes, including *S100a9*, *Mmp8*, *Vegfa*, and *Ccr2*, were comparable among the groups (Supplementary Fig. 1).

Assessment of ROS, NO, and arginase activity. To further characterize suppressive mediators of MDSCs induced under different conditions, we assessed ROS production, NO production, and arginase activity (Fig. 3). In two independent experiments, ROS-associated fluorescence was numerically higher in all induction groups than in the Control group (Fig. 3A). Representative flow cytometric histograms suggested increased NO-associated fluorescence in the CTX-containing groups (CTX and Tumor + CTX)

compared with the Control and Tumor groups (Fig. 3B). By contrast, arginase activity did not differ significantly among the groups, consistent with the absence of *Arg1* upregulation in the qRT-PCR analysis (Fig. 2C and 3C). Taken together, these results suggest that different induction conditions were characterized by distinct ROS- and NO-associated profiles.

RNA-seq analysis. RNA sequencing was performed on MDSCs isolated from the Control, Tumor, CTX, and Tumor + CTX groups (n = 4 mice per group). Principal component analysis (PCA) showed clear separation among the four groups, with PC1 and PC2 accounting for 55% and 23% of the total variance, respectively (Fig. 4A). Consistent with the PCA results, hierarchical clustering based on the top 1,000 most variable genes grouped the samples according to their respective induction conditions (Fig. 4B). Volcano plot analysis identified 2,283, 1,438, and 812 differentially expressed genes (DEGs) in the Tumor, CTX, and Tumor + CTX groups, respectively, compared with the Control group (Fig. 4C–E). The Tumor group therefore showed the largest number of DEGs, whereas fewer DEGs were detected in the Tumor + CTX group. The corresponding DEG lists are provided in Supplementary Table 2. Venn diagram analysis revealed both shared and group-specific upregulated and downregulated genes among the three induction conditions (Fig. 4F, G). Although some DEGs were common to all groups, each condition also contained a substantial set of unique DEGs, indicating that tumor growth, CTX treatment, and their combination produced overlapping but distinct transcriptional responses. qRT-PCR analysis of selected DEGs confirmed expression patterns consistent with the RNA-seq results (Fig. 5).

Pathway enrichment analysis. KEGG pathway analysis identified several significantly enriched pathways among upregulated genes, suggesting that pathway-level enrichment was relatively selective in each condition (Supplementary Fig. 2). In the Tumor group, upregulated genes were enriched in the JAK-STAT signaling pathway, efferocytosis, and cholesterol metabolism. In the CTX group, enriched pathways included the Fanconi anemia pathway, homologous recombination, and cell cycle. In the Tumor + CTX group, upregulated genes were associated with the JAK-STAT signaling pathway, cytokine-cytokine receptor interaction, pathways in cancer, and complement and coagulation cascades. By contrast, downregulated genes showed broader pathway enrichment across all groups, predominantly involving immune- and signaling-related pathways. GO enrichment analysis further supported condition-dependent differences among the groups (Supplementary Fig. 3). Together, these results indicate that tumor growth, CTX treatment, and their combination are associated with distinct pathway-level transcriptional signatures in MDSCs.

Discussion

In this study, we demonstrated that 4T1 tumor growth, CTX treatment, and their combination all promoted the expansion of bone marrow MDSCs but generated phenotypically and transcriptionally distinct MDSC populations. Consistent with previous studies, 4T1 tumor growth and CTX treatment preferentially expanded PMN-MDSCs and M-MDSCs, respectively (6, 10, 15). These differences in subset composition were accompanied by distinct mediator-associated profiles. Cells from the tumor-containing groups showed numerically higher ROS-associated fluorescence, whereas cells from the CTX-

containing groups showed an apparent increase in NO-associated fluorescence. At the transcriptional level, RNA sequencing separated the four groups and identified condition-specific transcriptional programs.

The preferential expansion of different MDSC subsets suggests that tumor growth and CTX treatment alter myelopoiesis through distinct mechanisms. In tumor-bearing mice, the increase in total leukocyte numbers is consistent with tumor-driven myelopoiesis and systemic inflammatory responses. GM-CSF, G-CSF, IL-6, and other inflammatory mediators have been implicated in MDSC expansion and granulocytic skewing in several tumor models (8, 11, 16, 17). In contrast, CTX treatment increased MDSCs without a corresponding increase in total leukocyte numbers. This pattern may reflect CTX-induced bone marrow injury and lymphopenia followed by compensatory hematopoietic recovery (12, 13). In the Tumor + CTX group, PMN-MDSCs were not significantly increased, whereas M-MDSCs were further expanded, suggesting that CTX-driven myelopoietic responses may exert a stronger influence on subset composition under the combined treatment protocol. These findings suggest that tumor growth and CTX treatment differ not only in the magnitude of MDSC expansion but also in the lineage bias of the MDSC populations they generate.

The differences in subset composition were accompanied by distinct profiles of immunosuppression-associated mediators. Tumor-induced cells showed increased *Cybb* expression together with a trend toward higher ROS-associated fluorescence, suggesting a molecular profile consistent with an increased capacity for oxidative activity. In contrast, cells from the CTX-containing groups showed limited changes in the selected canonical MDSC-associated genes but an apparent increase in NO-associated fluorescence compared with cells from the Control and Tumor groups. This discrepancy may reflect post-transcriptional or metabolic regulation of iNOS activity that was not captured by qRT-PCR. Notably, *Arg1* expression was reduced in the Tumor and CTX groups, whereas total arginase activity remained unchanged among groups. Although ARG1 is commonly regarded as a key mediator of MDSC-associated immunosuppression, its expression and functional contribution vary according to the cellular subset, induction signal, and tissue microenvironment (18, 19). The lack of *Arg1* induction and the absence of increased arginase activity may partly reflect the analysis of bone marrow-derived populations, which differ from splenic and tumor-resident MDSCs (20). Overall, these results suggest that arginase-related mechanisms were not a dominant feature of bone marrow MDSCs under the present experimental conditions, whereas ROS- and NO-associated profiles varied according to the induction context.

Interestingly, the Tumor + CTX group showed a marked increase in MDSCs together with preferential expansion of the M-MDSC subset. This group also exhibited a distinct gene expression profile, with *Tgfb1* and *Cd84* being significantly upregulated compared with the Control group. This profile may reflect the combined effects of tumor-derived inflammatory signals and CTX-induced tissue damage or hematopoietic stress.

RNA-seq analysis further revealed distinct transcriptional clusters for each induction condition, supporting the concept that the phenotypic and molecular characteristics of MDSCs are shaped by their induction context. In the Tumor group, enrichment of the JAK-STAT signaling pathway was consistent with exposure to tumor-derived cytokines and inflammatory signals that promote dysregulated myelopoiesis (16). The enrichment of efferocytosis and cholesterol metabolism pathways may further reflect metabolic and functional adaptation of tumor-induced myeloid populations. In contrast, CTX-induced cells showed enrichment of the Fanconi anemia pathway, homologous recombination, and cell-cycle-related pathways, which may reflect DNA damage responses and proliferative recovery following CTX-induced hematopoietic injury. The Tumor + CTX group exhibited enrichment of JAK-STAT signaling, cytokine-cytokine receptor interactions, and complement and coagulation cascades, suggesting a transcriptional state shaped by the combined influence of tumor-associated inflammation and treatment-related stress. Importantly, the clear separation of the CTX group by RNA sequencing, despite limited changes in the selected canonical MDSC-associated genes assessed by qRT-PCR, indicates that targeted marker analysis alone may underestimate broader induction-dependent molecular differences.

This study has several limitations. First, we analyzed only bone marrow MDSCs and did not examine MDSCs in the spleen, peripheral blood, or tumor microenvironment. Second, negatively selected MDSCs were not directly assessed by T-cell suppression assay. Third, RNA sequencing was performed on bulk MDSCs without separately analyzing the PMN-MDSCs and M-MDSCs. Thus, some transcriptional differences among the groups may partly reflect differences in subset composition. Fourth, ROS and NO measurements were based primarily on relative fluorescence.

Overall, our findings demonstrate that tumor growth, CTX treatment, and their combination generate phenotypically and transcriptionally distinct MDSC populations. These results emphasize that MDSCs induced by different experimental protocols should not be considered interchangeable, even when they are identified using similar surface markers. Careful consideration of the induction context will be important for interpreting MDSC biology across experimental systems and for selecting appropriate models in studies of tumor immunity and therapy-induced immunoregulation.

Declarations

Ethics approval

All animal experiments were approved by the Institutional Animal Care and Use Committee of Nagoya City University (approval no. 25–041) and were conducted in accordance with the institutional guidelines for the care and use of laboratory animals.

Consent to participate

Not applicable.

Consent for publication

Not applicable.

Competing interests

The authors declare that they have no competing interests.

Funding

This work was supported by the Outstanding Research Group Support Program of Nagoya City University (grant no. 2401101). M.M.A. was supported by a scholarship from the Egyptian Ministry of Higher Education through the Egypt-Japan University of Science and Technology (E-JUST).

Author Contribution

M.M.A., A.M.Y., and A.M.M. performed the majority of the experiments and collected the experimental data. M.H. performed the RNA-seq experiments. A.O., A.M.R.F.E.-B., E.E., M.Sh., and Y.M. contributed to RNA-seq data analysis and bioinformatics analyses. S.M.Z., K.M.M., and M.Su. contributed to additional experiments and data collection. M.M.A. analyzed and interpreted the experimental data and prepared the initial draft of the manuscript. M.L.S. contributed to the study design, interpretation of the data, supervision of the experimental work, and critical revision of the manuscript. H.O. conceived and designed the study, supervised and coordinated the overall project, interpreted the data, acquired funding, and critically revised and finalized the manuscript. All authors reviewed and approved the final manuscript.

Acknowledgement

This work was supported by the Outstanding Research Group Support Program of Nagoya City University (Grant No. 2401101). MMA gratefully acknowledges the financial support from a scholarship provided by the Egyptian Ministry of Higher Education (MoHE) through the Egypt-Japan University of Science and Technology (E-JUST). The authors used ChatGPT to assist with English-language editing and manuscript refinement. All content was reviewed and approved by the authors.

Data Availability

The RNA-sequencing datasets generated during the current study have been deposited in the NCBI Gene Expression Omnibus (GEO) under accession number GSE345520. All other data supporting the findings of this study are included in the article and its supplementary information files or available from the corresponding author upon reasonable request.

References

1. Nagaraj S, Youn JI, Gabrilovich DI. Reciprocal relationship between myeloid-derived suppressor cells and T cells. J Immunol. 2013;191:17–23. 10.4049/jimmunol.1300654.
2. Gabrilovich DI. Myeloid-Derived Suppressor Cells. Cancer Immunol Res. 2017;5:3–8. 10.1158/2326-6066.CIR-16-0297.
3. Hegde S, Leader AM, Merad M. MDSC: Markers, development, states, and unaddressed complexity. Immunity. 2021;54:875–84. 10.1016/j.immuni.2021.04.004.
4. Tcyganov E, Mastio J, Chen E, Gabrilovich DI. Plasticity of myeloid-derived suppressor cells in cancer. Curr Opin Immunol. 2018;51:76–82. 10.1016/j.coi.2018.03.009.
5. Bronte V, Brandau S, Chen SH, et al. Recommendations for myeloid-derived suppressor cell nomenclature and characterization standards. Nat Commun. 2016;7:12150. 10.1038/ncomms12150.
6. Ding ZC, Lu X, Yu M, et al. Immunosuppressive myeloid cells induced by chemotherapy attenuate antitumor CD4 + T-cell responses through the PD-1-PD-L1 axis. Cancer Res. 2014;74:3441–53. 10.1158/0008-5472.CAN-13-3596.
7. Hamilton MJ, Banath JP, Lam V, Lepard NE, Krystal G, Bennewith KL. Serum inhibits the immunosuppressive function of myeloid-derived suppressor cells isolated from 4T1 tumor-bearing mice. Cancer Immunol Immunother. 2012;61:643–54. 10.1007/s00262-011-1125-0.
8. Marvel D, Gabrilovich DI. Myeloid-derived suppressor cells in the tumor microenvironment: expect the unexpected. J Clin Invest. 2015;125:3356–64. 10.1172/JCI80005.
9. Roberts LM, Perez MJ, Balogh KN, Mingledorff G, Cross JV, Munson JM. (2022) Myeloid Derived Suppressor Cells Migrate in Response to Flow and Lymphatic Endothelial Cell Interaction in the Breast Tumor Microenvironment. Cancers (Basel). 14. 10.3390/cancers14123008
10. Youn JI, Nagaraj S, Collazo M, Gabrilovich DI. Subsets of myeloid-derived suppressor cells in tumor-bearing mice. J Immunol. 2008;181:5791–802. 10.4049/jimmunol.181.8.5791.
11. Waight JD, Hu Q, Miller A, Liu S, Abrams SI. Tumor-derived G-CSF facilitates neoplastic growth through a granulocytic myeloid-derived suppressor cell-dependent mechanism. PLoS ONE. 2011;6:e27690. 10.1371/journal.pone.0027690.
12. Salem ML, Al-Khami AA, El-Nagaar SA, Zidan AA, Al-Sharkawi IM, Marcela Diaz-Montero C, Cole DJ. Kinetics of rebounding of lymphoid and myeloid cells in mouse peripheral blood, spleen and bone marrow after treatment with cyclophosphamide. Cell Immunol. 2012;276:67–74. 10.1016/j.cellimm.2012.03.010.
13. Ding ZC, Aboelella NS, Bryan L, Shi H, Zhou G. The Monocytes That Repopulate in Mice After Cyclophosphamide Treatment Acquire a Neutrophil Precursor Gene Signature and Immunosuppressive Activity. Front Immunol. 2020;11:594540. 10.3389/fimmu.2020.594540.
14. Guo Q, Lv Z, Fu Q, Jiang C, Liu Y, Lai L, Chen Q, Shen J, Wang Q. IFN-gamma producing T cells contribute to the increase of myeloid derived suppressor cells in tumor-bearing mice after

cyclophosphamide treatment. Int Immunopharmacol. 2012;12:425–32. 10.1016/j.intimp.2011.12.016.

15. Talmadge JE, Gabrilovich DI. History of myeloid-derived suppressor cells. Nat Rev Cancer. 2013;13:739–52. 10.1038/nrc3581.
16. Li K, Shi H, Zhang B, Ou X, Ma Q, Chen Y, Shu P, Li D, Wang Y. Myeloid-derived suppressor cells as immunosuppressive regulators and therapeutic targets in cancer. Signal Transduct Target Ther. 2021;6:362. 10.1038/s41392-021-00670-9.
17. Abrams SI, Waight JD. Identification of a G-CSF-Granulocytic MDSC axis that promotes tumor progression. Oncoimmunology. 2012;1:550–1. 10.4161/onci.19334.
18. Rodriguez PC, Ochoa AC. Arginine regulation by myeloid derived suppressor cells and tolerance in cancer: mechanisms and therapeutic perspectives. Immunol Rev. 2008;222:180–91. 10.1111/j.1600-065X.2008.00608.x.
19. Grzywa TM, Sosnowska A, Matryba P, Rydzynska Z, Jasinski M, Nowis D, Golab J. Myeloid Cell-Derived Arginase in Cancer Immune Response. Front Immunol. 2020;11:938. 10.3389/fimmu.2020.00938.
20. Calvert RD, Fleet JC, Fournier PGJ, Juarez P, Burcham GN, Haverkamp JM, Guise TA, Ratliff TL, Elzey BD. Monocytic Myeloid-Derived Suppressor Cells from Tumor Tissue Are a Differentiated Cell with Limited Fate Plasticity. Immunohorizons. 2022;6:790–806. 10.4049/immunohorizons.2200079.

Figures

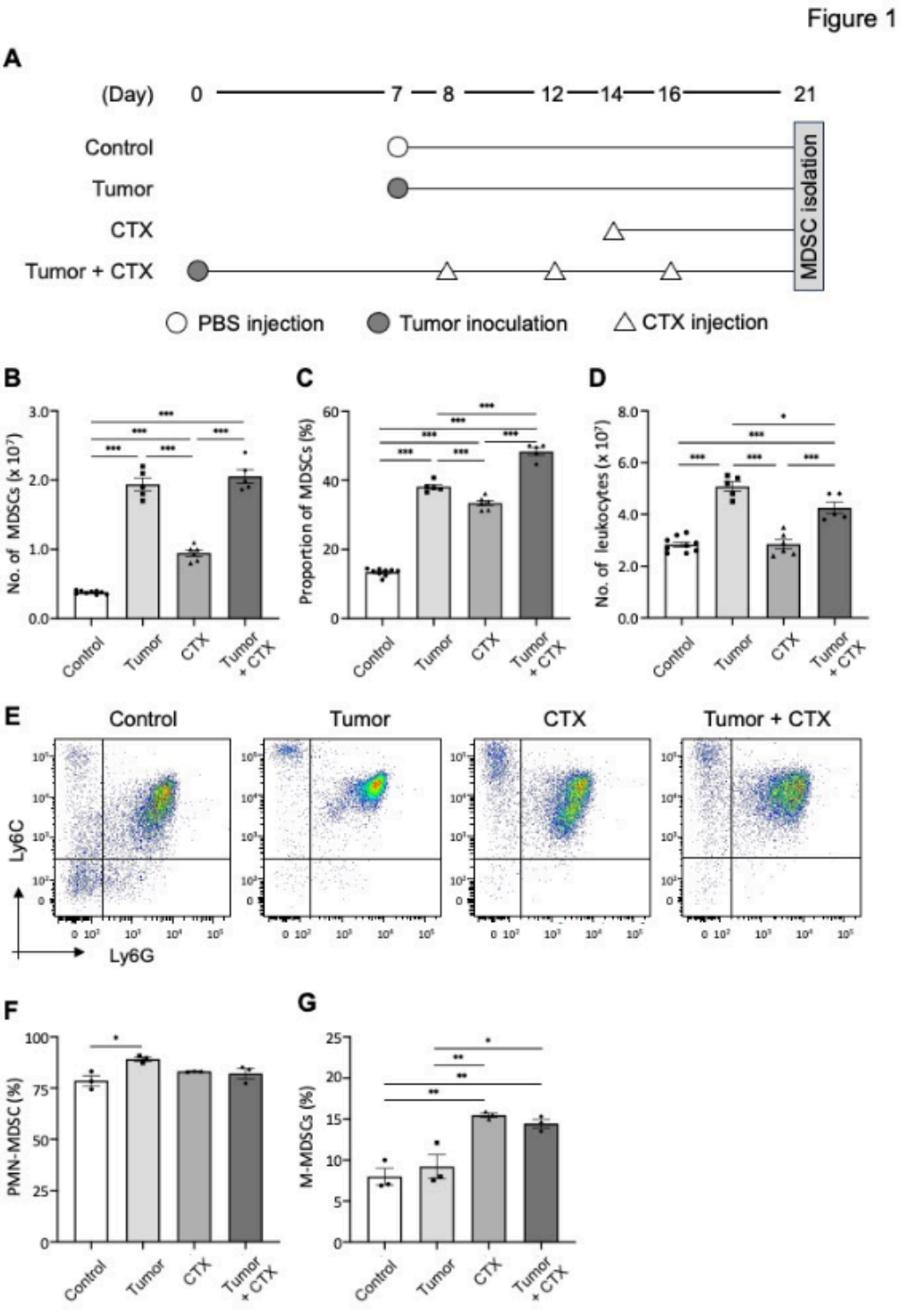

Figure 1

Differential expansion and subset composition of isolated bone marrow MDSCs induced under different conditions. (A) Experimental protocol for MDSC induction. **(B)** Total number of bone marrow MDSCs. **(C)** Proportion of MDSCs among bone marrow cells. **(D)** Total number of leukocytes. **(E)** Representative flow cytometry plots showing the PMN-MDSC and M-MDSC subsets. **(F)** Frequency of PMN-MDSCs. **(G)**

Frequency of M-MDSCs. Data are presented as mean ± SEM (n = 4 mice per group). *P < 0.05, **P < 0.01, ***P< 0.001.

Figure 2

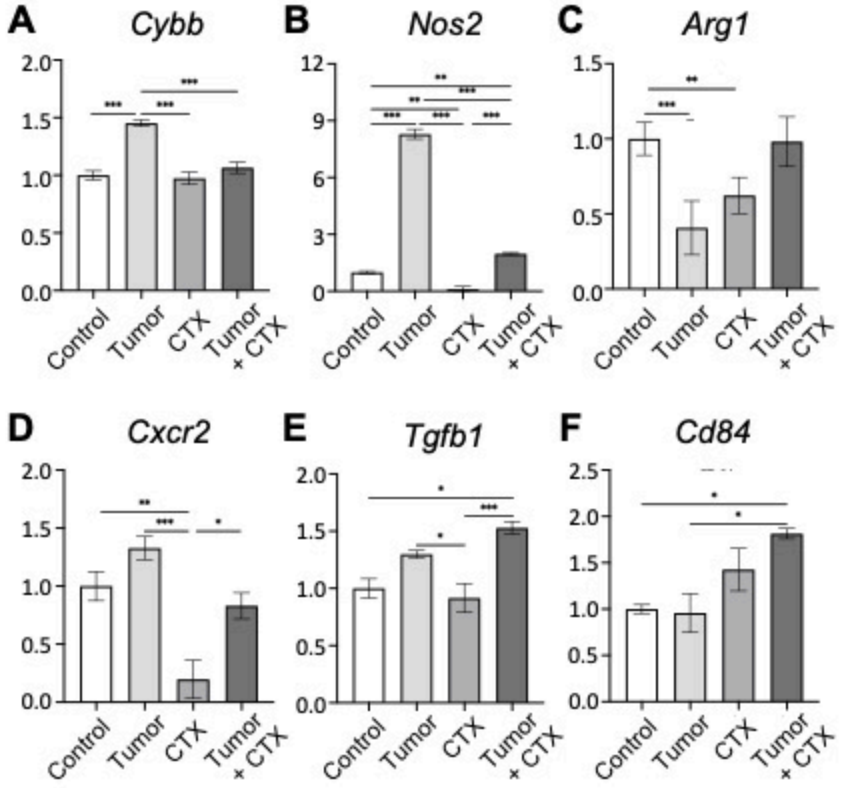

Figure 2

Expression of immunoregulatory genes in isolated bone marrow MDSCs. Gene expression levels are presented relative to the Control group. **(A)** *Cybb*. **(B)** *Nos2*. **(C)** *Arg1*. **(D)** *Cxcr2*. **(E)** *Tgfb1*. **(F)** *Cd84*. Data are presented as mean ± SEM (n = 4 mice per group). *P < 0.05, **P < 0.01, ***P < 0.001.

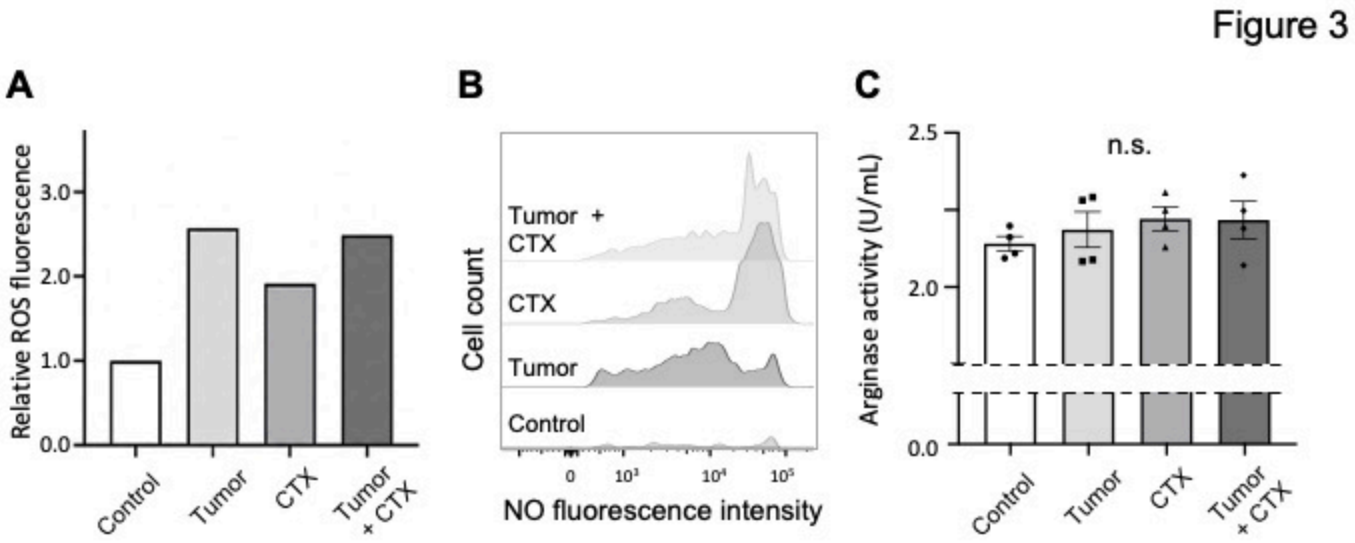

Figure 3

ROS, NO, and arginase activity in isolated bone marrow MDSCs. (A) Relative quantification of intracellular reactive oxygen species (ROS) fluorescence measured using DCFH-DA. Values were normalized to the Control group. Representative data from one of two independent experiments are shown. **(B)** Flow cytometric histograms of nitric oxide (NO)-related fluorescence measured using DAF-FM DA. Representative data from one of two independent experiments are shown. **(C)** Arginase activity (U/mL). Data are presented as mean ± SEM (n = 3 mice per group). n.s., not significant.

Figure 4

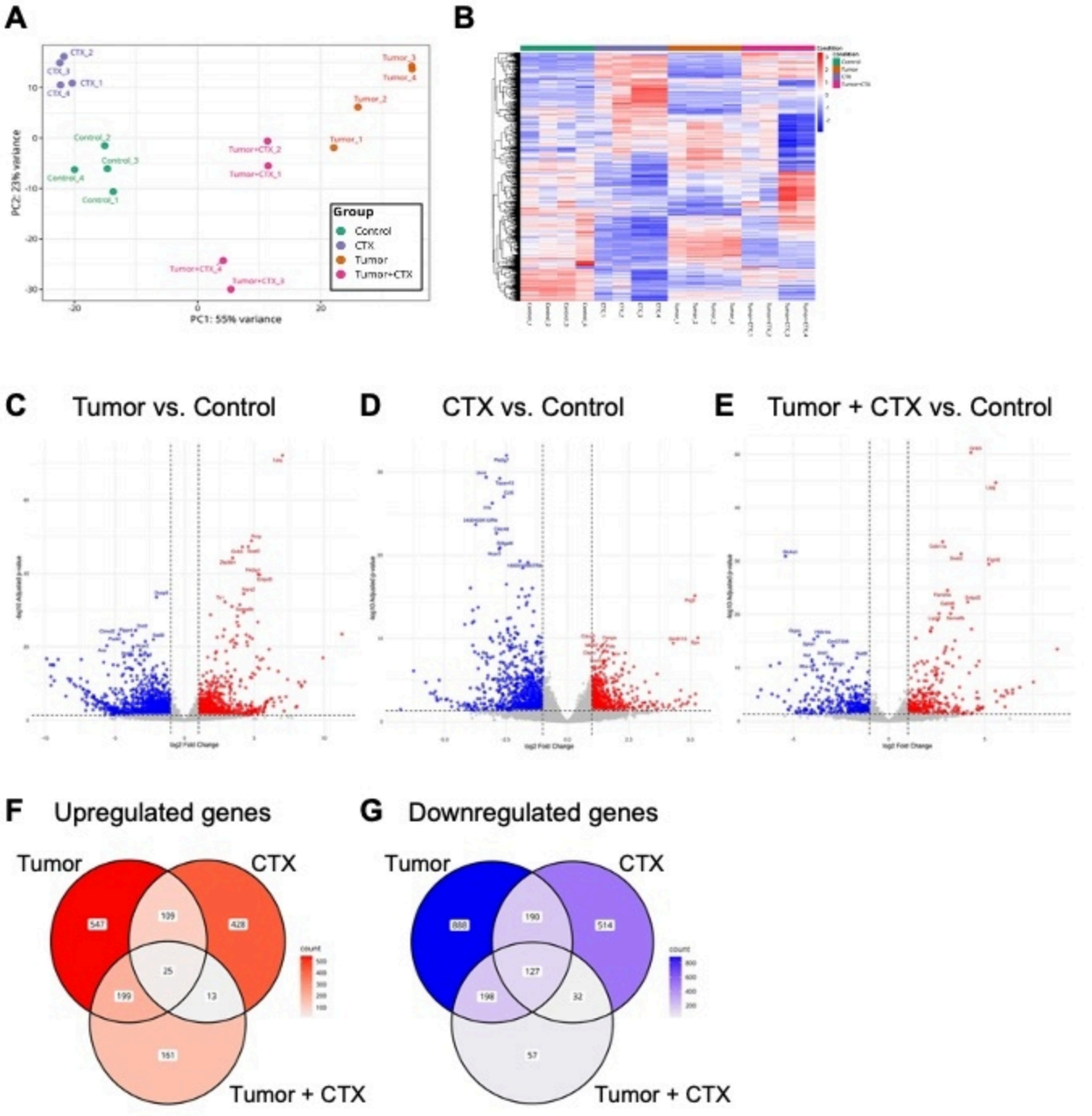

Figure 4

Transcriptomic profiling of isolated bone marrow MDSCs induced under different conditions. (A) Principal component analysis (PCA) of RNA-seq data from MDSCs isolated from the Control, Tumor, CTX, and Tumor + CTX groups. Each dot represents an individual biological replicate (n = 4 mice per group). **(B)** Hierarchical clustering heatmap of the top 1,000 most variable genes across all samples. **(C–E)** Volcano plots showing differentially expressed genes in the Tumor, CTX, and Tumor + CTX groups

compared with the Control group. Red and blue dots indicate significantly upregulated and downregulated genes, respectively. **(F, G)** Venn diagrams showing the overlap of upregulated genes **(F)** and downregulated genes **(G)**among the Tumor, CTX, and Tumor + CTX groups.

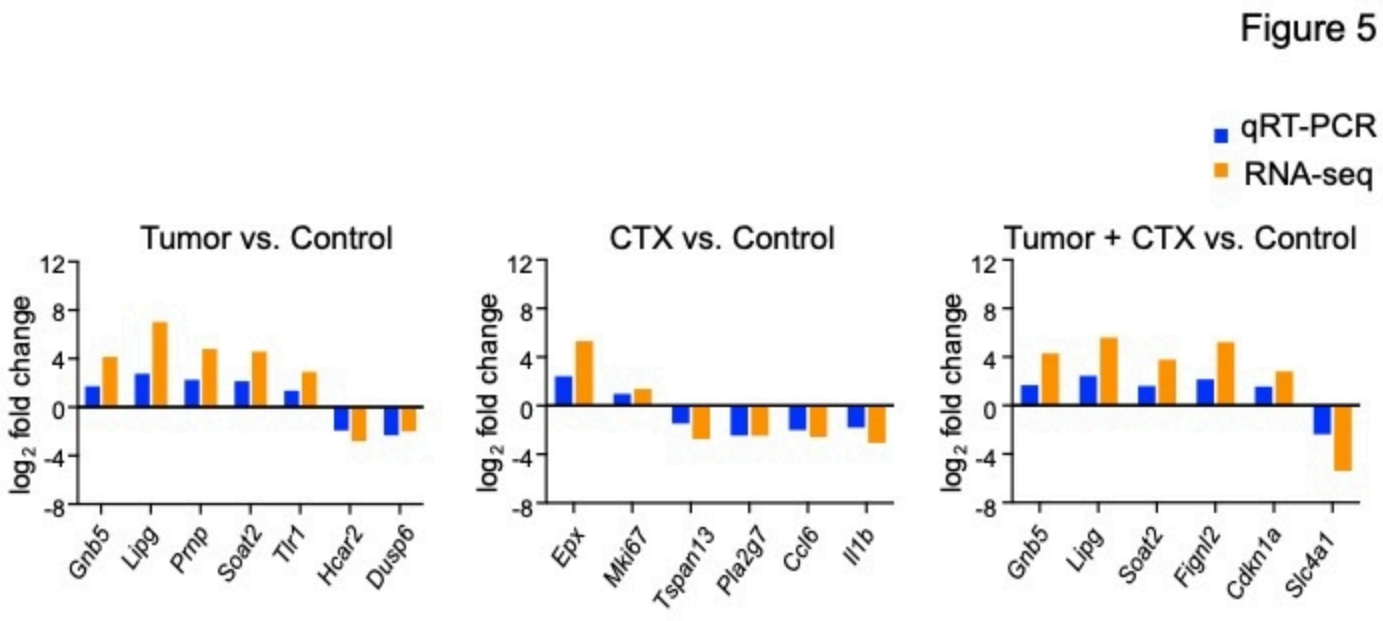

Figure 5

Validation of RNA-seq data by quantitative RT-PCR. Both qRT-PCR and RNA-seq values are presented as log2 fold changes relative to the Control group (n = 4 mice per group).

Supplementary Files

This is a list of supplementary files associated with this preprint. Click to download.

- SupplementaryTable1.xlsx
- SupplementaryFigure1.jpeg
- SupplementaryFigure2.jpeg
- SupplementaryFigure3.jpeg